EES Catalysis

Accepted Manuscript

This article can be cited before page numbers have been issued, to do this please use: K. Huang, Y. Yan, Y. Yu, T. Yang, L. Qiao, J. Tu, J. Sui, W. Cai, S. Liu and X. Zheng, *EES Catal.*, 2025, DOI: 10.1039/D5EY00040H.

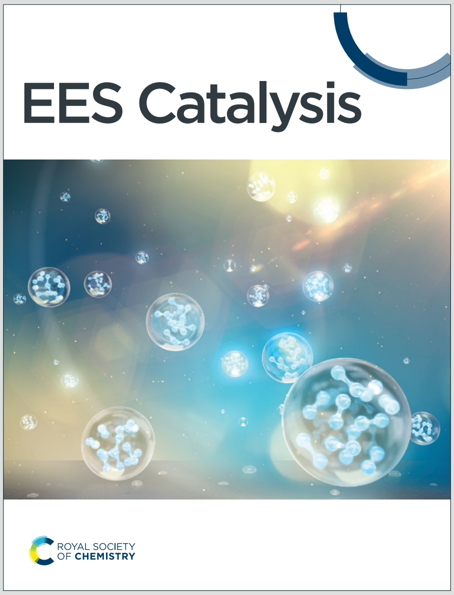

View Article Online
DOI: 10.1039/D5EY00040H

Broader context statement

The exploration towards efficient strategy for water oxidation electrocatalyst is vital for distributed mobile energy implementations (fuel cell, hydrogen refueling station, hydrogen energy vehicles etc.). CoO is considered to be potential metal compounds as OER electrocatalysts, due to rich Co crustal abundance, low materials cost and multiple valence states. However, the conductivity of CoO is usually insufficient, and the intrinsic activities for OER is far from ideal states. Nowadays, many progresses have been made for modulating nanosized cobalt oxides through compositional modification strategies, where the heteroatoms incorporation is a typical mainstream advanced technology. However, the OER performance modulation effect induced by composition optimization gradually enters the bottleneck stage. Magnetic field assisting catalytic process as typical external field control method owns potential for breaking through electrocatalysis performance limitations beyond composition optimization. The coupling of magnetic field assistance and heteroatoms incorporation will pave a bright way for breakthrough the bottleneck of catalytic performance and developing advanced cost-effective catalytic electrodes and devices, however, rare researches have explored this topic yet.

View Article Online
DOI: 10.1039/D5EY00040H

N, Fe co-incorporated CoO nanoarray enhanced by magnetic field for efficient water oxidation

Keke Huang[a], Yaotian Yan[a,*], Yaqiang Yu[a], Taili Yang[a], Liang Qiao[b], Jinchun Tu[c], Jiehe Sui[a], Wei Cai[a], Shude Liu[d*], Xiaohang Zheng[a*]

[a] *School of Materials Science and Engineering, Harbin Institute of Technology, Harbin 150001, China*

[b] *Key Laboratory of Materials Design and Quantum Simulation, College of Science, Changchun University, Changchun, 130022, China*

[c] *State Key Laboratory of Marine Resource Utilization in South China Sea, College of Materials and Chemical Engineering, Hainan University, Haikou 570228, China*

[d] *Engineering Research Center of Technical Textile, Ministry of Education, College of Textiles, Donghua University, Shanghai 201620, China*

*Corresponding author. Email: zhengxiaohang@hit.edu.cn (Xiaohang Zheng); sdliu@dhu.edu.cn (Shude Liu); ytyanhit@hit.edu.cn (Yaotian Yan)

View Article Online
DOI: 10.1039/D5EY00040H

Abstract

CoO as a typical water oxidation electrocatalyst has gradually entered the bottleneck stage of performance modulation through composition optimization. Herein, the N, Fe co-bonded CoO was achieved by N plasma, which suggests further potential to be enhanced by magnetic field during oxygen evolution reaction (OER) electrocatalysis. N atoms serve as bridge for bonding Fe centers and Co centers, which serves as fast channel for electron transfer. N, Fe co-doping decreases the electrons density around Co^{2+} centers, which increases the unpaired electrons for electrons acceptors. As a result, the intrinsic OER activities are boosted, which is further beneficial for amplifying the magnetic enhancement effect. The best performance emerges under parallel magnetic field with 420 mT intensity, which results in lowered overpotential of 217 mV and Tafel slope of 25.1 mV/dec in alkaline media. The magnetic enhancement comes from magnetohydrodynamic effect and the escape energy barrier reduction of paramagnetic triplet state O_2. The magnetic enhancement effect would be amplified when catalytic current becomes larger (magnetic current is 8 mA and 22 mA under 500 mA and 1000 mA total current respectively). This work provides an in-depth insight on magnetic enhancing mechanism, as well as a highly feasible strategy coupling heteroatoms with magnetic field to be operated for breaking through bottleneck of non-noble electrocatalysis performance.

Keywords: oxygen evolution reaction, charge transfer, electrocatalysis, magnetic enhancement, water oxidation

View Article Online
DOI: 10.1039/D5EY00040H

1. Introduction

The water oxidation electrocatalysis (OER) plays a vital role in distributed mobile energy implementations such as fuel cell, hydrogen refueling station, hydrogen energy vehicles[1]. However, the OER is composed of four-electron transfer steps, whose slow kinetics limited the total efficiency of related devices[2, 3]. Therefore, high performance electrocatalysts were demanded to facilitate the OER process. The commonly used electrocatalysts are IrO_2 and RuO_2, whose scarcity and high-cost block commercial applications[4]. Therefore, high-efficiency non-noble metal electrocatalysts were urged to be explored, which becomes a common concern for related fields[5].

3*d*-transition-metal oxides, typically CoO based compounds, have attracted lots of interest as potential OER electrocatalysts, due to rich Co crustal abundance, low materials cost and multiple valence states[6-8]. The unique di-μ-oxo bridged Co-Co coordination benefits for deprotonation process, where the formation of active oxygen ligand is promoted for boosting OER[9]. However, the conductivity of CoO is usually insufficient, and the intrinsic activities for OER is far from ideal states [10, 11]. To address above issue, plenty of efforts have been devoted to compositional design such as defect engineering [12], phase transition [13], and doping [14], which gradually enters the bottleneck stage for modulating OER performances. Recently, external magnetic fields have been reported highly effective for controlling fluid behavior and regulating ionic chemical reaction[15-17]. The nature of electrocatalytic water oxidation lies in the adsorption and transforming of a series intermediates ($OH^–$, $O^{2–}$, $OOH^{3–}$ and O_2 *etc.*). Importantly, the nature of paramagnetic triplet state of molecular oxygen means that the parallel electron spin directions in adjacent adsorbed oxygen (*O) would lower the formation energy barrier of O_2 product. Considering that the adsorption of *O on catalysts follows spin conservation rule between *O and active sites, unifying the spin direction of catalyst surface would be able to

View Article Online
DOI: 10.1039/D5EY00040H

induce spin parallel *O for boosting O_2 formation[18].

Previous researchers such as Xu *et al.*[9, 19-22] and Mascarós *et al.*[16] have made significant breakthroughs on interactions between external magnetic field and magnetic materials, revealing that the external magnetic could influence the spin orientation of solid surfaces. The stronger the magnetic properties of a solid, the more favorable it is for spin regulation. However, CoO is a weak magnetic substance[23], which means that the external magnetic field owns very limited effects on surface spin regulation. Utilizing strong magnetic Fe element to incorporate CoO may be a promising way to enhance the effect of external magnetic field on surface spin. However, the fine manipulation of high valence Fe^{3+} cations on oxide surface still remains challenge, cause that the electrostatic repulsion of Co and Fe cations results in unstable surface incorporation. Until recent, a few excellent studies about Fe-N coordination modes on carbon materials suggest that the half-filling *p* orbital in N induce rich valence states and bonding properties compared with O[24-27]. This inspires us that the N ligand can be utilized to bridge spin-polarized Fe cations on CoO surface. Therefore, the coupling of magnetic field with compositional modified electrocatalysts is expected to regulate the adsorption and transformation behaviors of intermediates, thus making breakthroughs for overcoming the bottleneck of OER performances. However, few attempts have been made in such aspects, and the integration of N and Fe heteroatoms with huge electronegativity difference on CoO surface remains big challenge.

To address above concerns, high-energy N atmosphere generated by plasma was utilized to anchor the Fe cations on CoO to form N-Fe-CoO nanoarrays, which suggests further potential to be enhanced by magnetic field during OER. N atoms serve as bridge for bonding Fe centers and Co centers, which serves as fast channel for electron transfer. N, Fe co-doping decreases the electrons density around Co^{2+} centers, which increases the unpaired electrons and holes for electrons acceptors in valence band. As a result, the intrinsic OER activities are boosted, which is further beneficial for amplifying the magnetic enhancement effect. The best performance emerges under parallel magnetic field with 420 mT intensity, which results in lowered overpotential of 217 mV and Tafel slope of 25.1 mV/dec in alkaline media.

2. Results and discussion

As shown in **Fig. 1a**, CoO prepared by hydrothermal is grown on carbon cloth in nanosheet structure, with the edge size of ~2 microns, but the thickness is extremely thin, at the nanometer level. The morphology of Fe-CoO in **Fig. 1b** is the same as the size of CoO, indicating that the Fe^{3+} ions treatment does not change the morphology of the sample. In addition, the N-Fe-CoO suggests the similar morphology as CoO in **Fig. 1c**, indicating that the N-plasma would not destroy the surface lamellar structure. Further, in order to determine the composition of the sample, the XRD test was used to analyze the phase of the sample, as shown in **Fig. 1d**. As can be seen from the figure, the diffraction peaks of the samples correspond to the standard CoO phase (JCPDS card no. 43-1004). No other peak positions were found, indicating that the CoO electrode derived by hydrothermal method is pure phase. The peak positions of N-Fe-CoO spectrum are consistent with those of CoO, and there is no other diffraction peak of Fe or N based compounds, which indicates that Fe and N atoms exist in the form of doping, rather than forming compounds. Moreover, the results of element mapping (**Fig. S2**) and X-ray photoelectron spectroscopy (XPS) XPS survey spectra (**Fig. S3**) reveal that the Co, O, Fe and N elements in N-Fe-CoO are evenly distributed in the nanoarray, and the atomic percentage of N and Fe is about 10.9% and 1.9%. Notably, the diffraction peak is not sharp, which means a low crystallinity of CoO phase. The low crystallinity often means the rich unsaturated coordination atoms, which is favorable for serving electrocatalytic OER.

View Article Online
DOI: 10.1039/D5EY00040H

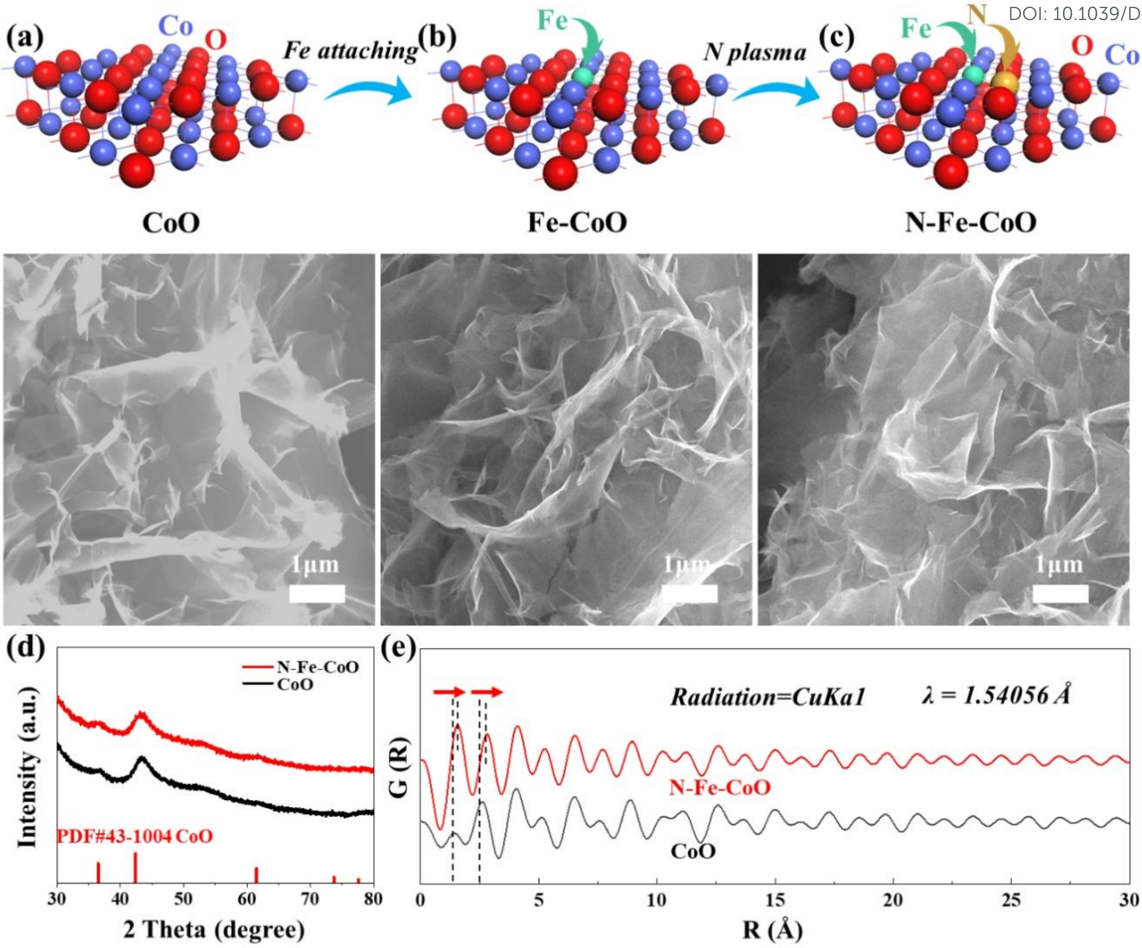

Fig. 1 The microstructures of (a) CoO, (b) Fe-CoO, (c) N-Fe-CoO. (d) The XRD patterns of CoO and N-Fe-CoO samples, (e) the pair distribution function (PDF) analysis for CoO and N-Fe-CoO nanosheets (derived under CuKa1 radiation, λ = 1.54056 Å).

To further confirm that the N and Fe heteroatoms are successfully introduced into CoO, the pair distribution function (PDF) analysis is conducted (**Fig. 1e**). The introduce of N and Fe atoms in CoO is expected to influence the bond length of surrounding coordination atoms. The first peak represents the shortest interaction distance of the atoms in the material, where the N-Fe-CoO nanosheets suggest a larger interaction distance than CoO nanosheets. This is also consistent with the structural relaxation result by density functional theory (DFT) calculation (**Fig. S4**), where the bond length of Co-N pair (~2.5 Å) and Fe-O pair (~2.0 Å) is obviously larger than Co-O pair (1.8 Å). The atoms interaction distance would cause change in surface chemical states and electronic structure, which can be confirmed by XPS in next section.

View Article Online
DOI: 10.1039/D5EY00040H

The TEM images show more detailed information about the microstructure of CoO and N-Fe-CoO nanosheets (**Fig. 2**). Compared with CoO (**Fig. 2a**), the surface of N-Fe-CoO is rougher (**Fig. 2c**), which results from the N plasma etching. Furthermore, the high-resolution TEM (HRTEM) images (**Fig. 2b and 2d**) show well-defined lattice fringes with d-spacings of ~0.20 nm and ~0.28 nm, which closely correspond to the (200) and (111) planes of CoO (JCPDS card no. 43-1004). Importantly, the sub-nanometer interface emerges after introducing N, Fe heteroatoms into CoO (marked by blue dashed line), which indicates that the bonding process of N and Fe atoms on CoO surface is accompanied by slight lattice reconstruction.

XPS was employed to investigate the chemical states and surface electronic structures of the synthesized catalysts. As shown in **Fig. 2e**, the Co $2p_{3/2}$ peak at 780.1 eV in CoO nanosheets is attributed to Co^{2+} [28, 29]. In Fe-CoO nanosheets, the Co^{2+} 2p3/2 peak shifts 0.4 eV towards a higher binding energy compared to CoO, suggesting that the strong electrostatic attraction of Fe^{3+} makes the outer electrons of Co atoms more likely to be released, reducing the electron density around Co centers. Meanwhile, compared to pure CoO, the binding energy of Co^{2+} $2p_{3/2}$ in N-CoO shows an increase of 1.4 eV. This shift implies that N-doping significantly alters the electronic structure of Co^{2+} centers, indicating a potential chemical bonding interaction between Co and N elements. N-Fe-CoO nanosheets exhibit the highest Co^{2+} $2p_{3/2}$ binding energy (781.9 eV), and the binding energy shift relative to CoO is approximately equal to the sum of the shifts for N-CoO and Fe-CoO, confirming the synergistic effect of N and Fe dopants. Besides, the Fe 2p spectra of Fe-CoO and N-Fe-CoO nanosheets are depicted in **Fig. 2g**, where six peaks are identified. Excluding the low-intensity satellite peak, the peaks at 711.3 eV and 724.4 eV in Fe-CoO are assigned to Fe^{2+}, while those at 714.3 eV and 727.2 eV correspond to Fe^{3+} [30, 31]. For

View Article Online
DOI: 10.1039/D5EY00040H

N-Fe-CoO, the peaks at 711.0 eV and 724.4 eV are attributed to Fe^{2+}, and those at 713.6 eV and 726.8 eV to Fe^{3+}. The binding energy of Fe $2p_{3/2}$ is shifted towards lower energy by ~0.2 eV compared to the Fe-CoO electrode, which indicates that the doping of N leads to an increase of electron density near the Fe atoms. This confirms the electrons transferring from Co center to Fe center. Furthermore, as shown in **Fig. 2i**, the EPR spectrum of CoO, N-CoO, Fe-CoO and N-Fe-CoO show a very broad line with a $g \approx 2.12$ that can be attributed to the high spin Co^{2+} (three unpaired electrons)[32-34]. In general, the intensity of the EPR signal is positively correlated with the number of unpaired electrons. Notably, the N-Fe-CoO sample exhibits the highest EPR signal intensity, suggesting that the number of unpaired electrons at the Co center increases following N and Fe co-doping. In addition, it can be observed that the EPR signal strength of N-CoO is slightly smaller than that of CoO, indicating that the introduction of N may reduce the unpaired electron density of Co by forming Co-N covalent bonds. Additionally, it is obvious that the Fe-CoO and N-Fe-CoO exhibit a distinct new peak at $g \approx 3.07$ in their EPR spectra (**Fig. 2i**), which can be assigned to the spin of Fe^{3+}(five unpaired electrons)[35]. This observation indicates that Fe doping introduces additional unpaired electrons into the CoO system. Considering that the OER follows the following pathways[36]:

$* + OH^- \rightarrow *OH + e^-$,

$*OH \rightarrow *O + H^+ + e^-$,

$*O + OH^- \rightarrow *OOH + e^-$,

$*OOH \rightarrow * + O_2 + H^+ + e^-$,

the whole process is composed of potential-consuming four-electron transfer steps, where the catalyst surface serves as an electron acceptor role. The increase of unpaired electrons benefits for increasing electron acceptors on the electrode surface. Besides, the unpaired electrons are favorable for responding external magnetic field, which is expected for boosting OER process.

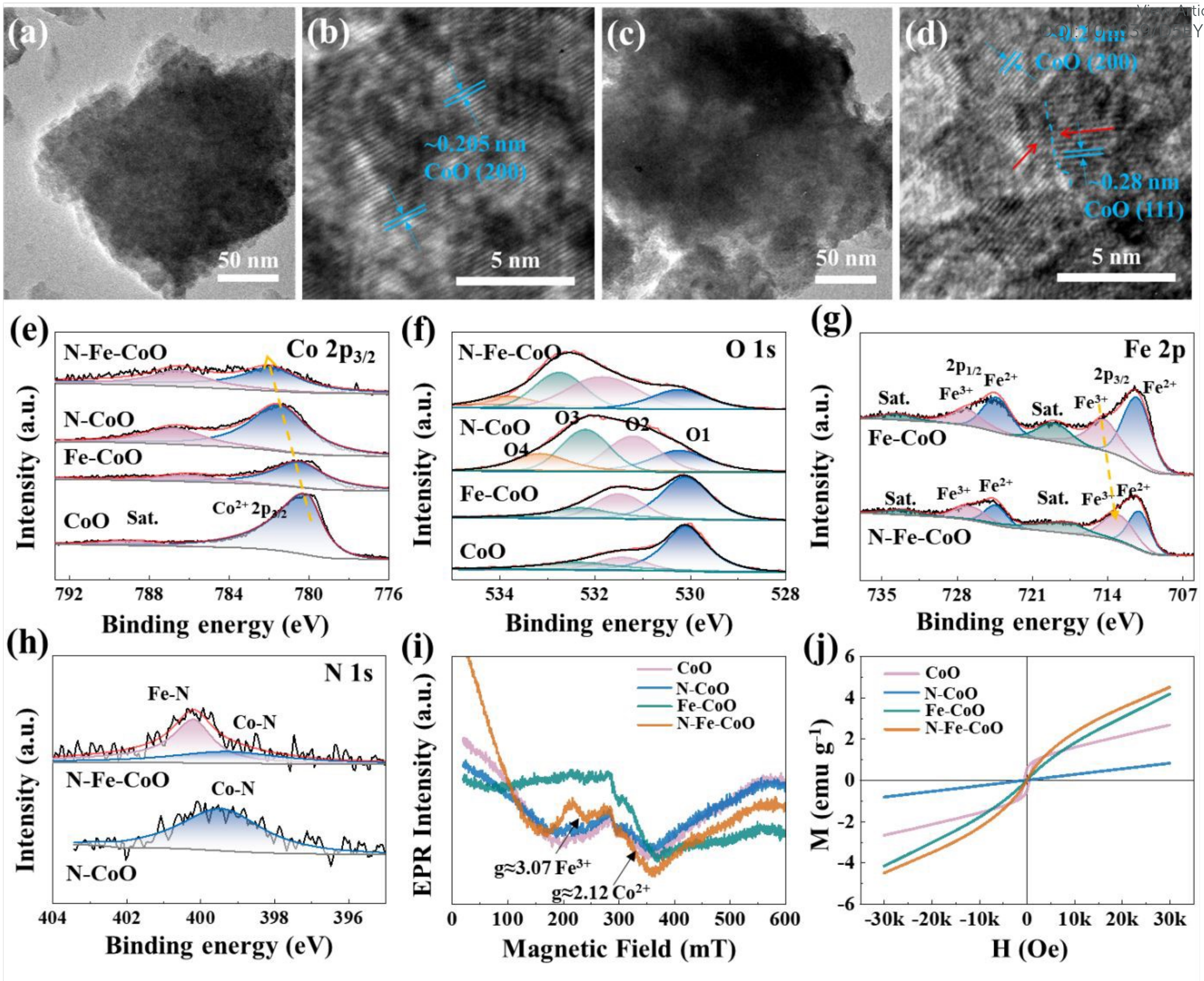

Fig. 2 The TEM characterizations of (a, b) CoO and (c, d) N-Fe-CoO samples, the blue dashed line marks the sub-nanometer interface. The (e) Co 2p XPS spectra and (f) O 1s spectra of as-prepared samples, (g) the Fe 2p XPS spectra of Fe-CoO and N-Fe-CoO samples, (h) the N 1s XPS spectra of N-CoO and N-Fe-CoO samples and the (i) EPR spectra (ν=9.84GHz) and (j) Magnetic hysteresis loops of CoO, N-CoO, Fe-CoO and N-Fe-CoO samples.

The O 1s spectra (**Fig. 2f**) of the samples were performed to investigate the surface defects of the catalysts. The O 1s spectra of CoO and Fe-CoO were fitted with three peaks corresponding to lattice oxygen (O1, 530.1 eV), defect sites with low oxygen coordination (O2, 531.4 eV), and hydroxyl groups or surface-adsorbed oxygen (O3, 532.3 eV)[37, 38]. Besides, the O 1s spectra of N-CoO and N-Fe-CoO reveal additional peaks at 533.2 eV and 533.4 eV, respectively, assigned to adsorbed water molecules (O4) on the surface. It is worth noting that the peak ratio of O2 and O3 increases after the electrode is doped with Fe and N. Importantly, the actual proportion of oxygen vacancies can be approximated by the peak area ratio of O2/(O1+O2+O3). According to the theoretical calculation, the O2 ratios of CoO, Fe-CoO, N-CoO and N-Fe-CoO are 16.8%, 27.3%, 35.5% and 42.7%, respectively. The results show that N plasma will produce more oxygen vacancy defects on the electrode surface. This is also one of the reasons for the improvement of OER activity, that is, oxygen vacancy can change the adsorption energy of the active species and enhance the intrinsic activity of the catalyst. **Fig. 2h** shows the N 1s spectra of the N-CoO and N-Fe-CoO electrodes. Only one obvious peak at 399.5 eV is identified from the N-CoO electrode, which is attributed to the Co-N bond[39]. However, two peaks can be obviously observed in the N-Fe-CoO electrode, the peak near 399.3 eV can be attributed to Co-N bond, and the peak around 400.2 eV can be attributed to Fe-N bond[40]. This indicates that N doping serves as a bridge for bonding Co and Fe centers, which benefits for accelerating electrons flowing and charge transferring during OER.

The magnetic hysteresis loops of CoO, N-CoO, and N-Fe-CoO at room temperature are also included, as shown in **Fig. 2j**. It is evident that N-CoO and N-Fe-CoO exhibit negligible hysteresis, indicating paramagnetic behavior (**Fig. S5**)[41]. In contrast, CoO shows a distinct hysteresis loop, characteristic of ferromagnetism[42]. From the hysteresis loop trend, it is evident that the saturation magnetization of N-CoO is lower than that of CoO. Combined with the EPR results, it can be speculated that this reduction may be attributed to the formation of covalent bonds between Co and N (Co-N), which decreases the density of unpaired electrons in Co and consequently reduces its magnetic moment contribution. Conversely, Fe-CoO demonstrates significantly higher saturation magnetization than CoO. This enhancement is likely due to the incorporation of Fe^{3+} ions, which introduce a large number of unpaired electrons into the CoO matrix following Fe doping. Notably, N-Fe-CoO may demonstrate a higher degree of magnetization compared to Fe-CoO. This observation diverges from the trend of saturated magnetization when N is doped in CoO, suggesting that the increase in saturated magnetization following N doping in Fe-CoO is closely associated with the interaction between Fe and N.

View Article Online
DOI: 10.1039/D5EY00040H

To explore the effects of magnetic field direction on OER performances of as prepared electrodes, herein, three magnetic field direction relative to electrode surface are tested: 90° (vertical), 45° and 0° (parallel). The polarization curves are shown in **Fig. 3a**. Compared with N-Fe-CoO electrode without magnetic field, the overpotential of N-Fe-CoO electrode with magnetic field is improved. As the Angle between the magnetic field and the electrode surface decreases, the overpotential decreases gradually. At 10 mA/cm^2 current density, the electrode overpotential was 221 mV without magnetic field, 220 mV when the magetic field was perpendicular to the electrode surface, 219 mV when the azimuth Angle was 45°. The lowest overpotential of 217 mV emerged when the magnetic field was parallel to the electrode surface. According to the electrochemical impedance spectrum (EIS) in **Fig. 3b**, the solution impedance and charge transfer resistance (R_{ct}) (reflected by semicircle diameter) are reduced after the magnetic field is applied. Then the effect of magnetic field intensity on the behavior of N-Fe-CoO electrode on oxygen evolution was investigated. During the test, the magnetic field is kept parallel to the electrode surface, and the magnetic field strength is changed by adjusting the distance between the magnet and the electrode. The polarization and EIS curves are shown in **Fig. 3c** and **3d**. The starting position value of the impedance spectrum first increases and then gradually decreases with the increase of the magnetic field strength, and the minimum value emerges when the magnetic field strength is 420 mT. This indicates that magnetic field affects the ions movement in solution. Based on this consideration, the polarization curves without IR correction can more truly reflect the effects of magnetic field strength on the OER performance. As shown in **Fig. 3c**, when the magnetic field intensity is 303 mT and 330 mT, the overpotential does not change; when the magnetic field increases to 370 mT, the overpotential decreases, and the overpotential continues to decrease as the magnetic field continues to increase.

View Article Online
DOI: 10.1039/D5EY00040H

In order to investigate the enhancing mechanism of magnetic field on OER more accurately, the N-Fe-CoO electrode is tested by chronoamperometry method. During the test, the magnetic field is applied (on) and removed (off) to determine the enhancement effect of the magnetic field. The constant voltages of 0.75 V and 0.8 V (relative to the reference electrode) are utilized. The time interval is unified as 300 s when there is no magnetic field to ensure the stability of the current, and then the magnetic field is applied to maintain the current for 300 s. This cycle is repeated three times to ensure that the magnetic field enhancement effect is not an accidental phenomenon. Since the patterns under potentials of 0.75 V (**Fig. 3e-h**) and 0.8 V (**Fig. 3i-l**) are similar, the following statements are based typically on 0.8 V potential. The initial current of the CoO electrode is ~99 mA, and applying a magnetic field induces a significant change in current, with a variation of ~1 mA, referred to as the "magnetic current" in subsequent analysis. For the Fe-CoO electrode, the initial current is slightly higher at ~109.5 mA. Under magnetic field enhancement, the current rises instantaneously to ~111 mA, resulting in a magnetic current of ~1.5 mA, which is marginally higher than that observed for the CoO electrode. The N-CoO electrode exhibits an initial stable current comparable to that of the Fe-CoO electrode, and the application of a magnetic field also induces a noticeable current change, with a magnetic current of ~1.5 mA. Notably, the N-Fe-CoO electrode demonstrates the highest initial current among the four electrodes, reaching ~127 mA. This observation confirms that co-doping with nitrogen (N) and iron (Fe) optimizes the electrocatalytic activity of CoO. Under magnetic field conditions, the current of the N-Fe-CoO electrode further increases to ~129 mA, with a magnetic current of ~2 mA, indicating the most pronounced magnetic enhancement effect among the tested electrodes.

The relationship between the magnetic current and the initial electrode current is revealed in the following bar chart (**Fig. S6**). Both the magnetic current and initial current of Fe-CoO and

View Article Online
DOI: 10.1039/D5EY00040H

N-CoO increase under the same potential, which indicates the N doping or Fe doping benefits for magnetic enhancement effect on OER. The magnetic current of N-Fe-CoO nanosheets is highest under the same potential, which confirms that the co-doping of N and Fe introduces the highest magnetic field enhancement for OER. To further analyze the enhancement effect of magnetic field on N-Fe-CoO electrode, the OER performance without magnetic field and with the optimum parameter of magnetic field (parallel to the electrode surface and the intensity is maximum) were analyzed in detail. As shown in **Fig. 3m**, the polarization curves showed that the overpotential at 10 mA/cm^2 was improved by 4 mV, from 221 mV to 217 mV. The Tafel slope obtained by processing the polarization curve is shown in **Fig. 3n**. The Tafel slope under the magnetic field is 25.1 mV/dec, which is smaller than the Tafel slope value of 27.3 mV/dec without the magnetic field. The magnetic field will accelerate the kinetics of OER reaction, which means that the improvement of current density can be amplified to a great degree when the magnetic field is applied at bigger potential or current conditions. This is confirmed by **Fig. 3o**, where the magnetic current density gradually increases with the increase of potential. At 1.505 V (vs. RHE), the enhanced magnetic current density is 10 mA/cm^2. Such improvement will be of great significance in practical applications. The EIS was further fitted[43, 44], as shown in **Fig. 3p**, the solution resistance R_s under the magnetic field was 1.466 Ω, which was 0.05 Ω lower than the R_s without the magnetic field of 1.516 Ω. The R_{ct} decreased from 0.173 Ω to 0.113 Ω. This indicates that the magnetic field not only promotes the material transport in solution, but also accelerates the charge transfer at the electrolysis interface[45].

View Article Online
DOI: 10.1039/D5EY00040H

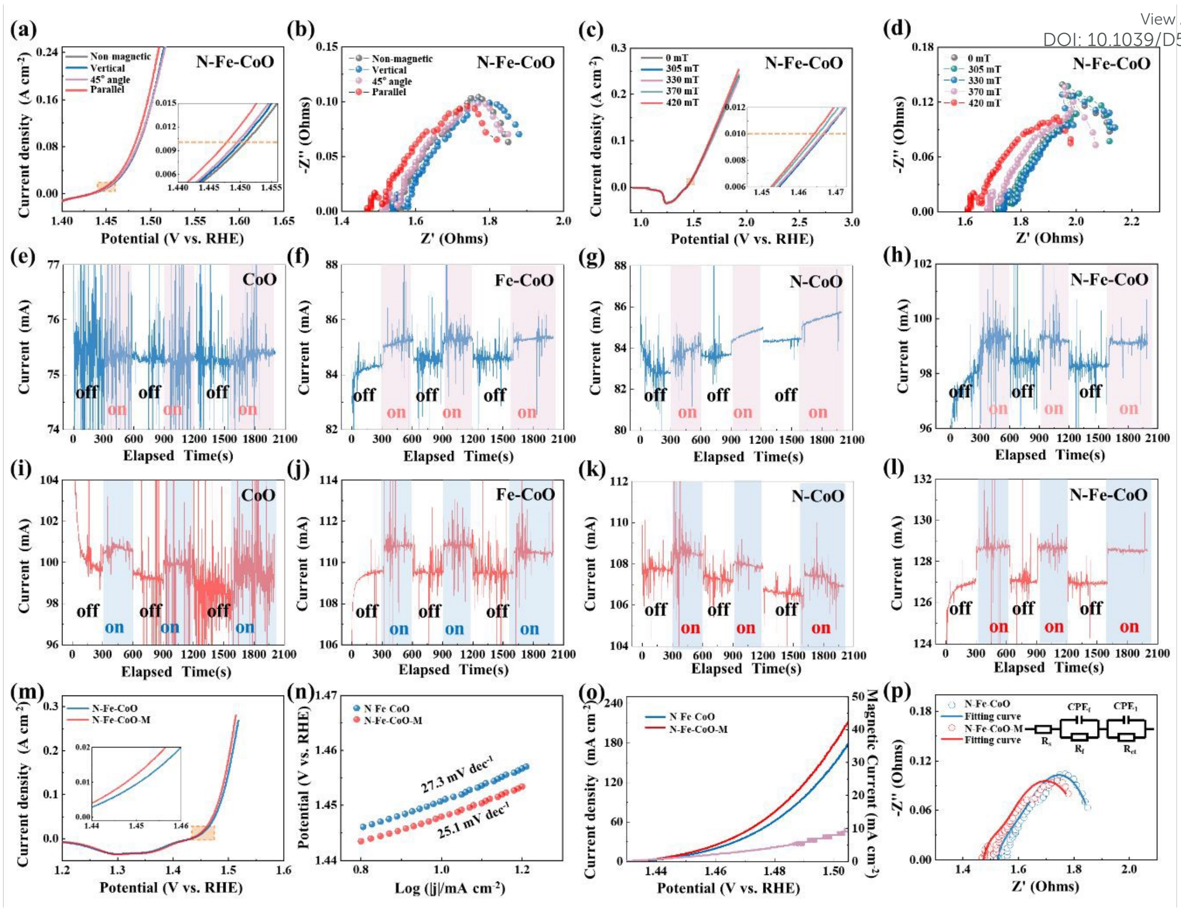

Fig. 3 (a) OER polarization curves and (b) electrochemical impedance spectroscopy of N-Fe-CoO under magnetic fields of different directions. The (c) OER polarization curves and (d) electrochemical impedance spectroscopy (EIS) of N-Fe-CoO under magnetic fields with different induction intensity. The chronoamperometry curves stimulated by parallel magnetic field under 0.75 V vs. Hg/HgO reference electrode of (e) CoO, (f) Fe-CoO, (g) N-CoO and (h) N-Fe-CoO. The chronoamperometry curves stimulated by parallel magnetic field under 0.8 V vs. Hg/HgO reference electrode of (i) CoO, (j) Fe-CoO, (k) N-CoO and (l) N-Fe-CoO. The comparison of (m) polarization curves, (n) Tafel slopes, (o) magnetically enhanced current curve and (p) EIS with corresponding fitting of N-Fe-CoO sample with and without magnetic field.

The process of catalytic reaction can be divided into electrode reaction and liquid phase mass transfer. Electrode reactions involve complex REDOX reactions, while liquid phase mass transfer is the process of continuously transporting reactants from solution to the electrode surface. Thus, the introduction of a magnetic field will be a combined effect, affecting the

View Article Online
DOI: 10.1039/D5EY00040H

electron reaction on the one hand and the transport of matter on the other. When the electric and magnetic fields exist simultaneously in the electrocatalytic system, the charged particles in the solution will be affected by both fields. The charged ions migrate directionally under the action of voltage. When the direction of movement is orthogonal to the magnetic field component, the Lorentz force will be exerted by the magnetic field. At this time, charged ions will change their original direction of movement, thus generating convection around the electrode, which is called magnetohydrodynamic effect (MHD). During the catalytic reaction, the solution near the electrode surface leads to concentration polarization due to the presence of concentration difference (diffusion layer). According to the Butler−Volmer equation, the concentration overpotential can be expressed as:

$$\varepsilon = \frac{RT}{nF}\ln\frac{I_d}{I_d - I}$$

the relationship between limiting current Id and diffusion layer thickness δ is given by Fick's first law:

$$I_d = nFD^{\frac{c}{\delta}}$$

where n is the number of transferred electrons, D is the diffusion coefficient, and c is the concentration of ions in the solution. However, the forced convection caused by magnetic field tends to destroy the diffusion layer thickness and strengthen the mass transfer process, thereby increasing the I_d and weakening the concentration polarization to reduce the concentration overpotential. More importantly, in the process of oxygen evolution, a large number of bubbles will be formed on the electrode surface as the reaction progresses. These gas products attached to the electrode surface would inhibit the effective active site of the electrode. The convective disturbance caused by the MHD effect can effectively alleviate the oversaturated accumulation of bubbles on the electrode surface, reduce the gas content in the electrolyte, increase the conductivity, and thus reduce the ohmic polarization. In addition, the MHD effect can

View Article Online
DOI: 10.1039/D5EY00040H

significantly reduce the coverage of bubbles on the electrode surface, avoiding the activation potential for additional active sites.

Fig. 4a describes the enhancement mechanism of CoO electrode OER performance by magnetic field. The magnetic field, electric field and Lorentz force are distributed in three dimensions and are orthogonal. When the electrode is undergoing OER, a magnetic field parallel to the surface of the electrode (orthogonal to the direction of the electric field) is applied externally. Under the magnetic field, the charged particles (OH^-) in the electrolyte will be subjected to the Lorentz force as shown in figure, which will cause the original motion direction to change and drive the fluid convection. Magnetic fluid acts on the electrode surface to accelerate the escape of gas molecules. Thus, concentration polarization, ohmic polarization and activation polarization can be effectively reduced. Based on this mechanism, it is easy to understand the influence of magnetic field direction and strength on electrochemical performance. When the magnetic field is perpendicular to the electrode surface, there is no MHD effect in the macroscopic solution, but there may be a small amount of microscopic MHD effect on the electrode surface, which will reduce the overpotential. With the change of Angle, the magnetic field component orthogonal to the electric field becomes larger and larger, and the magnetic field strength becomes larger and larger, and the MHD effect becomes stronger and stronger, so the overpotential improvement effect becomes more and more obvious. The magnetic enhancement effect of pure phase CoO and contrast samples can also be explained. At the same voltage, different catalysts have different intrinsic activities, resulting in different degrees of reaction. Less active electrocatalysts, such as CoO, have fewer bubbles on the surface and do not restrict the electrocatalytic reaction. However, for electrodes with high catalytic activity (such as N-Fe-CoO), the number of bubbles is excessive and cannot be removed in time without magnetic field, which becomes an obstacle to the process of oxygen evolution. Therefore, after

View Article Online
DOI: 10.1039/D5EY00040H

applying magnetic field, MHD effect can effectively alleviate this phenomenon, so that the overpotential has a great improvement. A further exploration about the effect of magnetic field on the N-Fe-CoO electrode intrinsic activity is conducted through DFT calculation. The atomic model of (200) plane is established (**Fig. 4b**) according to HRTEM characterization result shown in **Fig. 2**. The N-Fe-CoO suggests a typical metallic energy bands properties (**Fig. 4c**), where the obvious total density of states (TDOS) emerges near the Fermi level (**Fig. 4d**). This indicates the N, Fe incorporation ensures good electronic transmission properties. The isosurface of atomic deformation electron density distribution is calculated in **Fig. 4e**, and the red area and yellow area represent the surrounding electrons increasing and decreasing induced by N, Fe coupling respectively. The electrons around the Co and Fe centers decrease, while the electrons around the O and N centers increase. The N, Fe coupling in CoO caused some electrons delocalizing from Co/Fe centers to O/N centers. Thus, the average valence of Co, Fe atoms become higher, which is consistent with XPS analysis in **Fig. 3**. The positive shift of average valence benefits for forming hole channel to accept electrons from KOH electrolyte, as has been reported in previous research[46]. The simulation of magnetic field effect on catalytic process is based on the oxygen evolution mechanism shown in **Fig. 4f**, where adjacent *O bind to form the final O_2 product. When there is no magnetic field, the electron spin directions in N-Fe-CoO are chaotic, and the electron spin directions of adjacent *O are opposite (**Fig. 4g**). While applying magnetic field, the electron spin directions are forced to be consistent, therefore, the electron spin directions of adjacent *O are same. The escape free energy of O_2 molecule is calculated in **Fig. 4h**, which demonstrates that the magnetic field reduces the energy barrier for O_2 molecules to escape (from ~4.2 eV on CoO to ~1.5 eV on N-Fe-CoO), facilitating OER process.

View Article Online
DOI: 10.1039/D5EY00040H

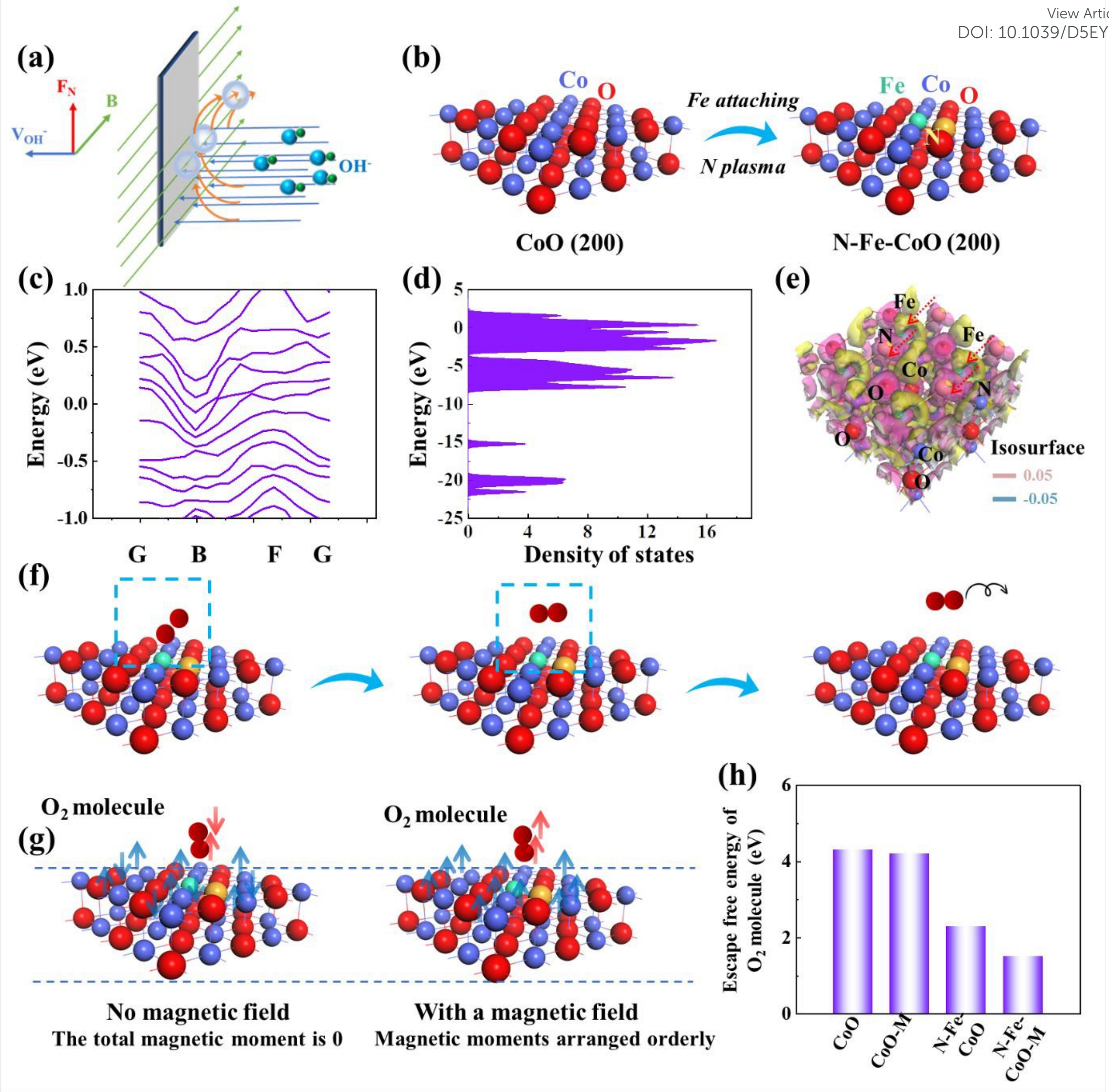

Fig. 4 (a) Schematic diagram of magnetic field enhancement mechanism for mass transfer during OER, (b) the established (200) atomic model for CoO and N-Fe-CoO, (c) the electronic energy band structure and (d) total density of states (TDOS) of N-Fe-CoO, (e) the isosurface of atomic deformation electron density distribution of N-Fe-CoO, the red arrow marks the local charge distribution after N, Fe introduction, (f) the sequence diagram of O_2 molecule escape process, (g) the adsorption of O_2 with or without a magnetic field, (h) the escape free energy of O_2 molecule without and with magnetic field.

Based on the understanding of the above mechanism, the magnetic response currents of the N-Fe-CoO electrode (2 cm × 4 cm) were tested at currents of 100 mA, 500 mA (high current) and 1000 mA (industrial current), respectively. The test results are shown in **Fig. 5**. When the

View Article Online
DOI: 10.1039/D5EY00040H

current of the electrode is 100 mA, the magnetic enhancement current is 2 mA. When the current is 500 mA, the magnetic enhancement current is 8 mA. When the current is 1 A, the magnetic enhanced current can reach 22 mA, showing a relatively ideal expected effect, which proves its potential in industrial production. In order to prove the MHD effect, we designed two different methods. If MHD effect exists, the gas bubbles will be driven and accelerated to detach. Therefore, if non-magnetic materials are selected as electrodes, by monitoring the rate of bubble detachment before and after applying a magnetic field during the catalytic process, one can determine the MHD effect. **Fig. 5d** shows the assembly method, and **Fig. 5e** shows that when non-magnetic platinum plates are used as electrodes, the situation before and after applying a magnetic field under constant potential. The peak spacing reflects the speed of bubble detachment. After applying a magnetic field, the peak spacing decreases, indicating that bubble detachment accelerates. Therefore, the MHD effect exists. Moreover, the non-magnetic carbon cloth substrate also suggests an obvious enhancement of catalytic performance (**Fig. 5f**), which also suggests the existence of MHD effect. In addition, the stability of the magnetic field enhancement effect and the stability of the catalyst electrode in the magnetic field were investigated. The electrode was tested at a current density of 10 mA/cm^2 for 12 h. As can be seen from **Fig. 5g**, the catalyst overpotential suggests stable potential during the work for 12 hours under the magnetic field. Comparing the potential values of the electrodes tested in the absence of magnetic field, the magnetic field enhancement remained stable within 12 h. The N-Fe-CoO electrocatalyst has bright commercial value, and the performance can be further enhanced by magnetic field, which provides new reference for industrial production.

View Article Online
DOI: 10.1039/D5EY00040H

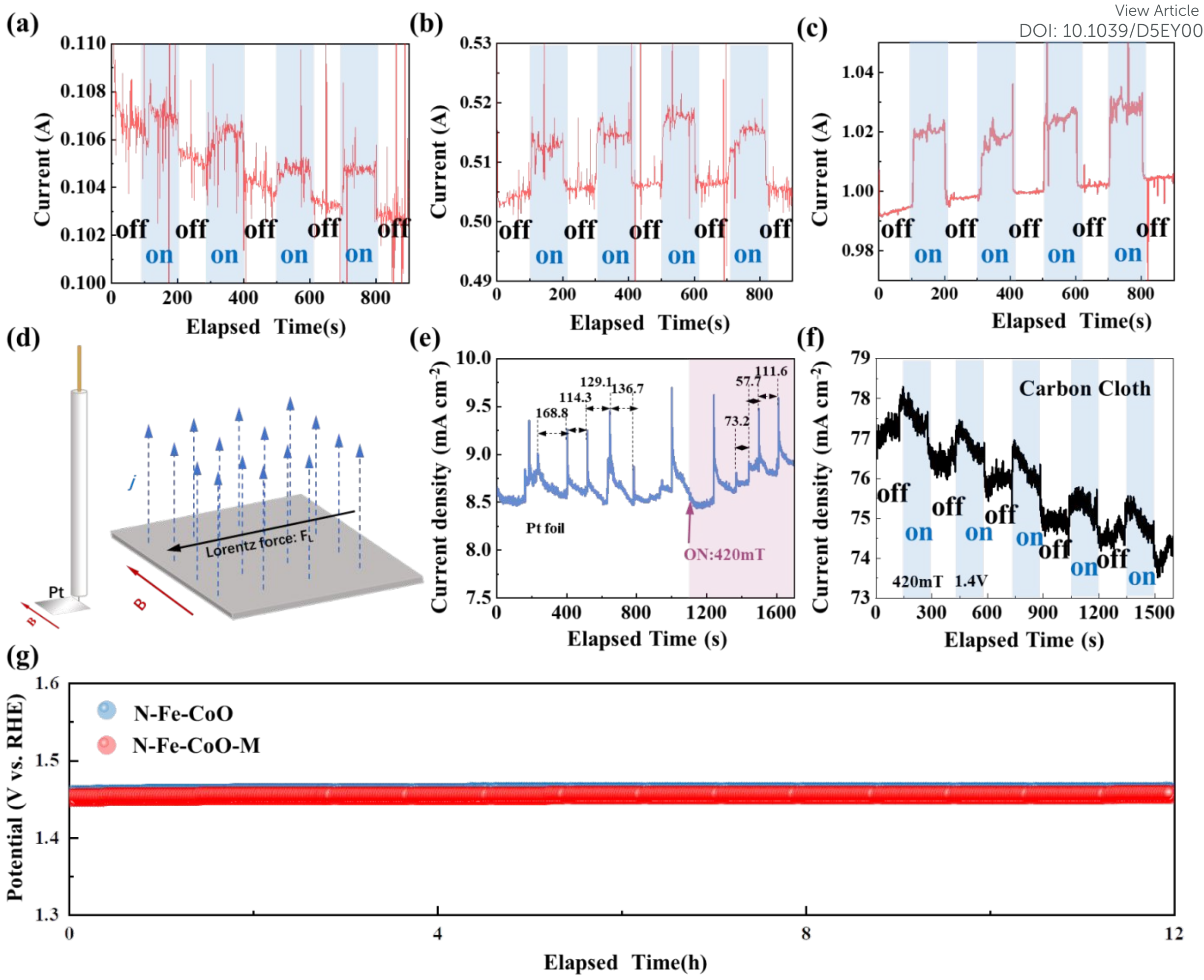

Fig. 5 The chronoamperometry curves of (a) 100 mA, (b) 500 mA and (c) 1000 mA stimulated by 420 mT parallel magnetic field; (d) MHD effect mechanism diagram; (e) the chronoamperometry curves of pure Pt foil electrode under the zero field or magnetic field (420 mT); (f) the chronoamperometry curves of pure carbon cloth electrode under the zero field or magnetic field (420 mT); (g) the chronopotentiometry analysis under 10 mA/cm^2 with and without magnetic field.

3. Experiment section

3.1 Setup of magnetic field enhanced electrocatalysis system

The electrocatalytic performance of N-Fe-CoO electrode was studied under magnetic field. Electromagnet (WD-80, TINDUN) was used as magnetic field generator. The intensity and orientation of the magnetic field can be easily tuned by adjusting the direction and the distance between magnet and samples (**Fig. S1**). During the test, the magnetic field is applied near the

View Article Online
DOI: 10.1039/D5EY00040H

working electrode, as shown in the schematic diagram of **Fig. 6a**. The relationship between the magnetic induction intensity and distance from magnet surface is shown in **Fig. 6b**, where a linear relationship can be observed, which is the reference for adjusting the magnetic induction intensity at the electrode. As for the direction, **Fig. 6c** suggests the reference of parallel direction.

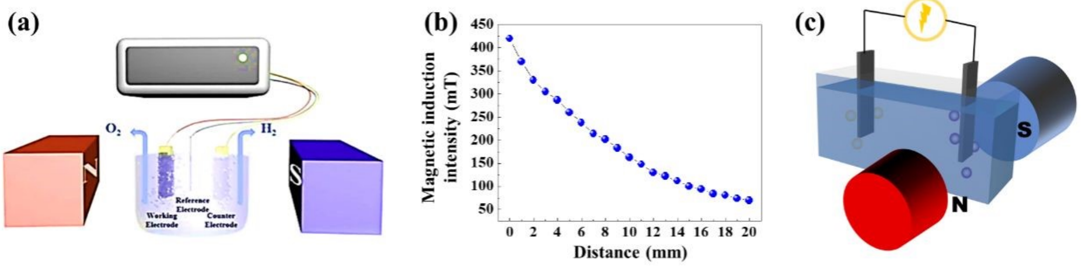

Fig. 6 (a) The illustration of electrolysis of water for oxygen evolution assisted by an external magnetic field; (b) the magnetic induction intensity versus magnet distance function curve; (c) the reference of parallel direction.

3.2 Synthesis of CoO nanosheets

The carbon cloth was first treated with concentrated nitric acid at 100°C for 3 h to generate hydrophilicity, then washed with deionized water and ethanol for several times and dried in air. The treated carbon cloth was placed into a mixed solution containing 2.3 g $Co(NO_3)_2{\cdot}6H_2O$, 3.2 g hexamethylenetetramine and 60 mL deionized water. The mixture was then transferred to the reaction kettle and kept at 120°C for 6 hours. The obtained samples were washed several times with deionized water and ethanol, and then dried at 60°C. The above samples were placed in a tubular furnace and heated to 250°C at a rate of 2°C/min under Ar atmosphere for 2 hours. Finally, pure phase CoO is obtained.

3.3 Synthesis of N-Fe-CoO nanosheets

Firstly, the prepared CoO nanosheet electrode (2 cm × 5 cm) was prepared, and then was immersed in the $FeCl_3{\cdot}6H_2O$ solution (4 mmol in 30 mL deionized water). After 30 s immersion treatment, the electrode sheet was completely infiltrated into the solution, and then the electrode was removed into the Plasma Enhanced Chemical Vapor Deposition (PECVD) device for plasma interaction under the atmosphere of nitrogen plasma. The specific experimental parameters are as follows: the experimental temperature is 300℃, the N_2 atmosphere flow is 50 sccm, the plasma reflector power is 300 W, and the pressure is 0.5 torr under low vacuum conditions. For ease of presentation, the prepared sample is denoted as N-Fe-CoO.

3.4 Synthesis of N-CoO sample

In order to compare and show the doping effect of N element, the sample without Fe immersion treatment was prepared, without changing other experimental parameters, which was abbreviated as N-CoO here.

3.5 Synthesis of Fe-CoO sample

In addition, in order to compare and show the doping effect of Fe element, the sample without N plasma treatment was prepared without changing other experimental parameters, which was abbreviated as Fe-CoO here.

4. Conclusion

The N, Fe co-bonded CoO was simultaneously achieved through one-step high-energy N plasma atomsphere, which suggests a bright potential to be enhanced by magnetic field during OER electrocatalysis. N atoms serve as bridge for bonding Fe centers and Co centers, which provides fast channel for electron transfer. The coupling of N, Fe co-doping decreases the electrons density around Co^{2+} centers, which increases the unpaired electrons for electrons acceptors. As a result, the intrinsic OER activities are boosted, which is further favorable for amplifying the magnetic enhancement effect. The best performance emerges under parallel

View Article Online
DOI: 10.1039/D5EY00040H

magnetic field with 420 mT intensity, which results in lowered overpotential of 217 mV and Tafel slope of 25.1 mV/dec in alkaline media. The magnetic enhancement comes from magnetohydrodynamic effect and the escape energy barrier reduction of paramagnetic triplet state O_2, which benefits for lowering both charge transferring resistance and mass transferring resistance. The magnetic enhancement effect would be amplified when catalytic current becomes larger (magnetic current is 8 mA and 22 mA under 500 mA and 1000 mA total current respectively). Current method affords unique advantages as OER activities amplifier and is feasible for industrial operation.

Conflicts of interest

There are no conflicts to declare.

Data availability

The data that support the findings of this study are available within the main text and supplementary Information.

Acknowledgement

This work was financially sponsored by National Natural Science Foundation of China (Grant No. 52471199 and No. 52302223), the Postdoctoral Fellowship Program of CPSF under Grant Number GZB20240949, Natural Science Foundation of Heilongjiang Province (LH2024E031), Heilongjiang Postdoctoral Fund (LBH-Z24174), State Key Laboratory of Precision Welding & Joining of Materials and Structures (24-R-01), Heilongjiang Touyan Team Program, Heilongjiang Province Science and Technology Special Fund (2024ZXDXA19), Hainan Province Science and Technology Special Fund (No. ZDYF2024SHFZ082). Special thanks to HIT Center of Analysis Measurement and Computing and Dr. Zheng Zhen for the electron microscope test analysis.

View Article Online
DOI: 10.1039/D5EY00040H

Reference

1. H. Tüysüz, *Accounts Chem Res*, 2024, **57**, 558-567.
2. X. H. Xie, L. Du, L. T. Yon, S. Y. Park, Y. Qiu, J. Sokolowski, W. Wang and Y. Y. Shao, *Adv. Funct. Mater.*, 2022, **32**, 2110036.
3. X. R. Ren, Y. Y. Zhai, N. Yang, B. L. Wang and S. Z. Liu, *Adv. Funct. Mater.*, 2024, **34**, 2401610.
4. F. L. Lyu, Q. F. Wang, S. M. Choi and Y. D. Yin, *Small*, 2019, **15**, 1804201.
5. M. N. Lakhan, A. Hanan, A. Hussain, I. A. Soomro, Y. Wang, M. Ahmed, U. Aftab, H. Y. Sun and H. Arandiyan, *Chem. Commun.*, 2024, **60**, 5104-5135.
6. Q. M. Sun, Y. W. Zhao, X. D. Yu, C. Zhang and S. X. Xing, *J. Electrochem. Soc.*, 2022, **169**, 060537.
7. M. S. Kim, M. A. Abbas, R. Thota and J. H. Bang, *J. Mater. Chem. A*, 2019, **7**, 26557-26565.
8. J. X. Guo, D. Y. Yan, K. W. Qiu, C. Mu, D. Jiao, J. Mao, H. Wang and T. Ling, *J. Energy Chem.*, 2019, **37**, 143-147.
9. T. Z. Wu, X. Ren, Y. M. Sun, S. N. Sun, G. Y. Xian, G. G. Scherer, A. C. Fisher, D. Mandler, J. W. Ager, A. Grimaud, J. L. Wang, C. M. Shen, H. T. Yang, J. Gracia, H. J. Gao and Z. C. J. Xu, *Nat. Commun.*, 2021, **12**, 3634.
10. R. Q. Li, P. F. Hu, M. Miao, Y. L. Li, X. F. Jiang, Q. Wu, Z. Meng, Z. Hu, Y. Bando and X. B. Wang, *J. Mater. Chem. A*, 2018, **6**, 24767-24772.
11. X. M. Fan, Y. Y. Fan, X. Zhang, L. Tang and J. X. Guo, *J. Alloy Compd.*, 2021, **877**, 160279.
12. J. F. Xie, H. Zhang, S. Li, R. X. Wang, X. Sun, M. Zhou, J. F. Zhou, X. W. Lou and Y. Xie, *Adv. Mater.*, 2013, **25**, 5807.
13. J. Hu, S. W. Li, J. Y. Chu, S. Q. Niu, J. Wang, Y. C. Du, Z. H. Li, X. J. Han and P. Xu, *ACS Catal.*, 2019, **9**, 10705-10711.
14. H. Y. Jin, X. Liu, S. M. Chen, A. Vasileff, L. Q. Li, Y. Jiao, L. Song, Y. Zheng and S. Z. Qiao, *ACS Energy Lett.*, 2019, **4**, 805-810.

View Article Online
DOI: 10.1039/D5EY00040H

15. J. D. Yao, W. J. Huang, W. Fang, M. Kuang, N. Jia, H. Ren, D. B. Liu, C. D. Lv, C. T. Liu, J. W. Xu and Q. Y. Yan, *Small Methods*, 2020, **4**, 2000494.

16. F. A. Garces-Pineda, M. Blasco-Ahicart, D. Nieto-Castro, N. Lopez and J. R. Galan-Mascaros, *Nat. Energy*, 2019, **4**, 519-525.

17. Y. Y. Zhang, C. Liang, J. Wu, H. Liu, B. Zhang, Z. X. Jiang, S. W. Li and P. Xu, *ACS Appl. Energ. Mater.*, 2020, **3**, 10303-10316.

18. Z. Fang, W. T. Zhao, T. Shen, D. P. Qiu, Y. C. Lv, X. M. Hou and Y. L. Hou, *Precis Chem*, 2023, **1**, 395-417.

19. Y. M. Sun, X. Ren, S. N. Sun, Z. Liu, S. B. Xi and Z. C. J. Xu, *Angew. Chem. Int. Edit.*, 2021, **60**, 14536-14544.

20. Y. M. Sun, S. N. Sun, H. T. Yang, S. B. Xi, J. Gracia and Z. C. J. Xu, *Adv. Mater.*, 2020, **32**, 202003297.

21. T. Wang, J. Y. Wang, Y. M. Sun, Y. Duan, S. N. Sun, X. Hu, S. B. Xi, Y. H. Du, C. Wang and Z. C. J. Xu, *Appl. Catal. B-Environ.*, 2019, **256**, 117844.

22. X. Ren, T. Z. Wu, Y. M. Sun, Y. Li, G. Y. Xian, X. H. Liu, C. M. Shen, J. Gracia, H. J. Gao, H. T. Yang and Z. J. Xu, *Nat. Commun.*, 2021, **12**, 2608.

23. G. Li, P. Wang, C. Y. Li, Z. Fang, M. He, W. W. Wang, X. L. Yuan, H. Li, P. G. Li and Z. X. Li, *Mater Res Lett*, 2022, **10**, 744-753.

24. T. Marshall-Roth, N. J. Libretto, A. T. Wrobel, K. J. Anderton, M. L. Pegis, N. D. Ricke, T. Van Voorhis, J. T. Miller and Y. Surendranath, *Nat. Commun.*, 2020, **11**, 5283.

25. C. Q. Li, C. S. He, F. Z. Sun, M. C. Wang, J. H. Wang and Y. Q. Lin, *Acs Appl Nano Mater*, 2018, **1**, 1801-1810.

26. R. Jiang, L. Li, T. Sheng, G. F. Hu, Y. G. Chen and L. Y. Wang, *J. Am. Chem. Soc.*, 2018, **140**, 11594-11598.

27. L. Jiao, J. K. Li, L. L. Richard, Q. Sun, T. Stracensky, E. R. Liu, M. T. Sougrati, Z. P. Zhao, F. Yang, S. C. Zhong, H. Xu, S. Mukerjee, Y. Huang, D. A. Cullen, J. H. Park, M. Ferrandon, D. J. Myers, F. Jaouen and Q. Y. Jia, *Nat. Mater.*, 2021, **20**, 1385.

28. Y. Y. Li, L. Zhang, J. H. Peng, W. Zhang and K. Peng, *J. Power Sources*, 2019, **433**, 226704.

29. R. Zhang, Y. Lu, L. Wei, Z. G. Fang, C. H. Lu, Y. R. Ni, Z. Z. Xu, S. Y. Tao and P. W.

View Article Online
DOI: 10.1039/D5EY00040H

Li, *J. Mater. Sci.-Mater. El.*, 2015, **26**, 9941-9948.

30. D. Friebel, M. W. Louie, M. Bajdich, K. E. Sanwald, Y. Cai, A. M. Wise, M. J. Cheng, D. Sokaras, T. C. Weng, R. Alonso-Mori, R. C. Davis, J. R. Bargar, J. K. Norskov, A. Nilsson and A. T. Bell, *J. Am. Chem. Soc.*, 2015, **137**, 1305-1313.
31. B. M. Hunter, N. B. Thompson, A. M. Muller, G. R. Rossman, M. G. Hill, J. R. Winkler and H. B. Gray, *Joule*, 2018, **2**, 747-763.
32. N. L. A. Rodin, M. R. Sahar and F. Mohd-Noor, *J Magn Magn Mater*, 2020, **496**, 165931.
33. M. Al-Ghoul, H. El-Rassy, T. Coradin and T. Mokalled, *J Cryst Growth*, 2010, **312**, 856-862.
34. S. K. Misra, S. I. Andronenko, S. S. Rao, J. Chess and A. Punnoose, *J Magn Magn Mater*, 2015, **394**, 138-142.
35. E. Balan, T. Allard, B. Boizot, G. Morin and J. P. Muller, *Clay Clay Miner*, 1999, **47**, 605-616.
36. Y. L. Pan, X. M. Xu, Y. J. Zhong, L. Ge, Y. B. Chen, J. P. M. Veder, D. Q. Guan, R. O'Hayre, M. R. Li, G. X. Wang, H. Wang, W. Zhou and Z. P. Shao, *Nat. Commun.*, 2020, **11**, 2002.
37. L. Y. Wu, Q. L. Wu, Y. Han, D. D. Zhang, R. R. Zhang, N. Song, X. F. Wu, J. R. Zeng, P. Yuan, J. Chen, A. J. Du, K. K. Huang and X. D. Yao, *Adv. Mater.*, 2024, **36**, 2401857.
38. J. Yang, S. Y. Hu, Y. R. Fang, S. Hoang, L. Li, W. W. Yang, Z. F. Liang, J. Wu, J. P. Hu, W. Xiao, C. Q. Pan, Z. Luo, J. Ding, L. Z. Zhang and Y. B. Guo, *ACS Catal.*, 2019, **9**, 9751-9763.
39. X. L. Hu, X. Chen, X. Li and C. H. Xu, *Adv. Funct. Mater.*, 2024, **34**, 2316699.
40. Q. A. Song, M. Li, X. S. Hou, J. C. Li, Z. J. Dong, S. Zhang, L. Yang and X. Liu, *Appl. Catal. B-Environ.*, 2022, **317**, 121721.
41. J. G. Zhao, M. Yang and Z. H. Hua, *J Magn Magn Mater*, 2014, **371**, 10-13.
42. A. Tomou, D. Gournis, I. Panagiotopoulos, Y. Huang, G. C. Hadjipanayis and B. J. Kooi, *J Appl Phys*, 2006, **99**, 123915.
43. Y. T. Yan, P. C. Wang, J. H. Lin, J. Cao and J. L. Qi, *J. Energy Chem.*, 2021, **58**, 446-462.

View Article Online
DOI: 10.1039/D5EY00040H

44. Y. T. Yan, J. H. Lin, T. Liu, B. S. Liu, B. Wang, L. Qiao, J. C. Tu, J. Cao and J. L. Qi, *Corros. Sci.*, 2022, **200**, 110231.

45. Y. T. Yan, J. H. Lin, T. X. Xu, B. S. Liu, K. K. Huang, L. Qiao, S. D. Liu, J. Cao, S. C. Jun, Y. Yamauchi and J. L. Qi, *Adv. Energy Mater.*, 2022, **12**, 2200434.

46. Y. Yan, K. Huang, J. Lin, T. Yang, P. Wang, L. Qiao, W. Cai and X. Zheng, *Appl. Catal. B-Environ.*, 2023, **330**, 122595.

View Article Online
DOI: 10.1039/D5EY00040H

Data availability

The data that support the findings of this study are available within the main text and supplementary Information.